Proceedings of the 37th International Conference on Ocean, Offshore & Arctic Engineering
OMAE2018
June 17-22, 2018, Madrid, Spain

OMAE2018-78250

STUDY OF HYDRODYNAMIC FORCES ON COMPLEX STRUCTURES

Ann-Sofie Bjørke
NOV Flexibles
Priorparken 480
DK-2605 Brøndby, Denmark

Erik Damgaard Christensen[1]
DTU-MEK
Nils Koppels Alle, Build. 403
DK-2800 Kgs. Lyngby,Denmark
[1]Contact Author

Stefan Carstensen
DTU-MEK
Nils Koppels Alle, Build. 403
DK-2800 Kgs. Lyngby,Denmark

Kasper Pagh Petersen
Ramboll
Hannemanns Allé 53
DK-2300 Copenhagen,
Denmark

Xerxes Mandviwalla
DTU-MEK
Nils Koppels Alle, Build. 403
DK-2800 Kgs. Lyngby, Denmark

Trygve Kristiansen
NTNU
Otto Nielsens veg 10
7491 Trondheim, Norway

Rolf Baarholm
Statoil ASA
Strandveien 4
NO-7500 Stjørdal, Norway

ABSTRACT

This paper presents a study on the interaction of structural members that can be related to a complex structure placed in a moonpool. The complex structure in the moonppol was simplified with varying number of members. The study has been carried out as a two-dimensional numerical study with supporting physical experiments. The focus was on the forces on the individual members as well as the entire structure. Additional the flow field associated with the oscillating water column in the moonpool was also studied.

INTRODUCTION

A large porous structure can be many things including armour- and filter layers in rubble mound breakwaters, cover- and protection layers for scour protection and equipment for the offshore industry. One important offshore application is the process of lowering a structure into a moonpool where the forces on the structure heavily affects the damping of the water.

Many survey, installation and diver support vessels are equipped with a moonpool, which is a large hole on the hull of the vessel. The moonpool serves as an access route for equipment such as Remotely Operated Vehicles, diving bells and subsea structures to enter the sea, as an alternative to vessel side crane operations. The use of a moonpool operation will reduce the forces on the equipment due to the pitch and roll motions of the vessel compared to a vessel side operation [1]. However, sloshing in the moonpool, caused by wave action and vessel motion, may still pose a risk in the operation. The primary concern is the so-called piston mode sloshing where the water body in the moonpool oscillates vertically as a rigid body. The amplitude of the motions can become very large under resonant conditions. For this reason, operational limitations are imposed on moonpool operations.

A significant amount of research has previously been performed on the subject. Piston mode moonpool sloshing has been described by, amongst others, [2] and [3]. Marintek (SINTEF Ocean) has developed a computational tool PVC3D for this purpose, see for instance [4], [5]. The studies indicated that potential theory severely overestimates the amplitude of the piston mode motion because significant damping will be present due to viscous effects such as separation at the inlet. In order to account for this, PVC3D combines potential flow modelling of the free wave surface with a full Navier-Stokes solution in areas where viscous effects are expected to be present.

The objective of the study presented in this paper was to study forces exerted on structures placed in a moonpool experiencing resonant piston mode sloshing. The methodology was based on numerical analyses of simplified representation of structures in a moonpool. To assist the numerical analyses additional physical model experiments were carried out. The focus of the study was on forces on individual members of the overall complex structure, the total force on the structure and the flow characteristics. Eventually, it could be argued that a complex structure resembles a porous structure. Then another approach can be followed as described in [6]. However, for less complex structures the interaction with waves can result in

complicated flow patterns in itself as seen in for instance [7] and [8].

THE NUMERICAL MODEL

In this section the numerical model used for the prediction of forces on structures in a moonpool is described. First we present the governing equations along with the chosen turbulence model. This is followed by a description of the numerical approach to solving the governing equations where a description of the specific OpenFOAM set-up used in the study is also found.

RANS equations

The numerical method is based on a solution of the Reynolds Averaged Navier-Stokes (RANS) equations that for the continuity equation and for the momentum equations read:

$$\frac{\partial U_i}{\partial x_i} = 0 \tag{1.1}$$

$$\frac{\partial U_i}{\partial t} + U_j \frac{\partial U_i}{\partial x_j} = -\frac{1}{\rho}\frac{\partial p}{\partial x_i} + \frac{\partial}{\partial x_j}\left((\nu + \nu_t)\left(\frac{\partial U_i}{\partial x_j} + \frac{\partial U_j}{\partial x_i}\right)\right) \tag{1.2}$$

where U_i is the time averaged velocity in the i[th] direction, p is the pressure, ν is the kinematic viscosity, and the ν_t is the eddy viscosity.

The eddy viscosity arises from the closure problem during the averaging process. Here the Reynolds stresses were modelled based on the eddy viscosity concepts, meaning that the Reynolds stresses could be modelled as:

$$\tau_{ij} = \rho\overline{u_i u_j} = \rho\nu_t\left(\frac{\partial U_i}{\partial x_j} + \frac{\partial U_j}{\partial x_i}\right) \tag{1.3}$$

In eqs. (1.3) the eddy viscosity still have to be found. To this end, a rather standard two-equation turbulence model was used, the SST *k-ω*-model(SST: Shear Stress Transport), see [9]. This model has shown to give robust and reliable solutions to the flow field where adverse pressure gradient has to be considered. For the sake of completeness we also present the model equations for the turbulent kinetic energy, *k*, and the specific dissipation rate ω here:

$$\rho\frac{\partial k}{\partial t} + \frac{\partial \rho k U_i}{\partial x_j} = \frac{\partial}{\partial x_j}\left[\left(\mu + \mu_t/\sigma_k\right)\frac{\partial k}{\partial x_j}\right] + \tau_{ij}\frac{\partial U_i}{\partial x_j} - \rho\beta^* k\omega \tag{1.4}$$

$$\rho\frac{\partial \omega}{\partial t} + \frac{\partial \rho\omega U_i}{\partial x_j} = \frac{\partial}{\partial x_j}\left[\left(\mu + \mu_t/\sigma_\omega\right)\frac{\partial \omega}{\partial x_j}\right] + \frac{\gamma}{\nu_t}\tau_{ij}\frac{\partial U_i}{\partial x_j} - \beta\rho\omega^2 + 2(1-F_1)\frac{\rho\sigma_{\omega 2}}{\omega}\frac{\partial k}{\partial x_j}\frac{\partial \omega}{\partial x_j} \tag{1.5}$$

The constants σ_k, and σ_ω are found from the generic equation (1.6), where numbers 1, and 2 corresponds to the inner and outer regions. The constants, γ, β, β^*, σ_k, and σ_ω, for the inner and outer solutions can be found in table 1 and 2:

$$\phi = F_1\phi^1 + (1-F_1)\phi^2 \tag{1.6}$$

The blending function F_1 is a function of the distance to the wall:

$$F_1 = \tanh(\arg_1^4)$$

where

$$\arg_1 = \min\left[\max\left(2\frac{\sqrt{k}}{0.09\omega z};\frac{500\mu}{z^2\omega}\right);\frac{4\rho k}{(CD_{k\omega})z^2\sigma_{\omega 2}}\right] \tag{1.7}$$

with

$$(CD_{k\omega}) = \max\left(2\rho\frac{1}{\sigma_{\omega 2}\omega}\frac{\partial k}{\partial x_j}\frac{\partial \omega}{\partial x_j};10^{-20}\right)$$

Table 1. Model constants for inner 'wall' region

β_1	β^*	γ_1	σ_{k1}	$\sigma_{\omega 1}$
0.075	0.09	0.553	2.0	2.0

Table 2. Model constants for outer 'surface' region

β_2	β^*	γ_2	σ_{k2}	$\sigma_{\omega 2}$
0.0828	0.09	0.4404	1.0	1.17

Finally, the following equation estimates the eddy viscosity used in the RANS-equations:

$$\nu_t = \frac{a_1 k}{\max(a_1\omega, \Omega F_2)} \tag{1.8}$$

Where Ω is the rotation ($\Omega = (\frac{\partial U_i}{\partial x_j} + \frac{\partial Uj}{\partial x_i})$), and a_1 is a constant. F_2 is a blending function which is one for boundary layer flows and zero for free shear layers. Equation (1.8) ensures that the original eddy viscosity is only used outside the inner layer where adverse pressure gradients are rare.

$$F_2 = \tanh(\arg_2^2)$$

where (1.9)

$$\arg_2 = \max(2\frac{\sqrt{k}}{0.09\omega z};\frac{500\mu}{z^2\omega})$$

Solution method

The solution method is based on the open source library OpenFOAM (Open Field Operation and Manipulation): This is an open source, object-orientated C++ library for numerical simulations of fluid dynamics. The equations were solved on the computational mesh using a velocity-pressure solver. The numerical integration in time was based on the PISO-algorithm using a Euler backward time integration. The Gauss linear Upwind (LUD) resolved the convective terms, while central differences was used for diffusive terms. This leads to a spatial resolution close to second order. The pressure equation that can be derived from the continuity equation was solved using Geometric-Algebraic Multi-Grid solver (GAMG), while the momentum equations and the turbulence equations were solved using preconditioned bi-conjugate gradient solver (PBICG). As

preconditioner the incomplete LU (DILU) was used for the momentum and turbulence equations. More information can be found in [10].

The computational grid

The computational domain was resolved by a number of computational cells forming the computational mesh. Figure 1 shows the meshing strategy. Closest to the structure, in this case a square cylinder, we find the finest resolution. As we go further away from the structure coarser resolution of the computational domain was used.

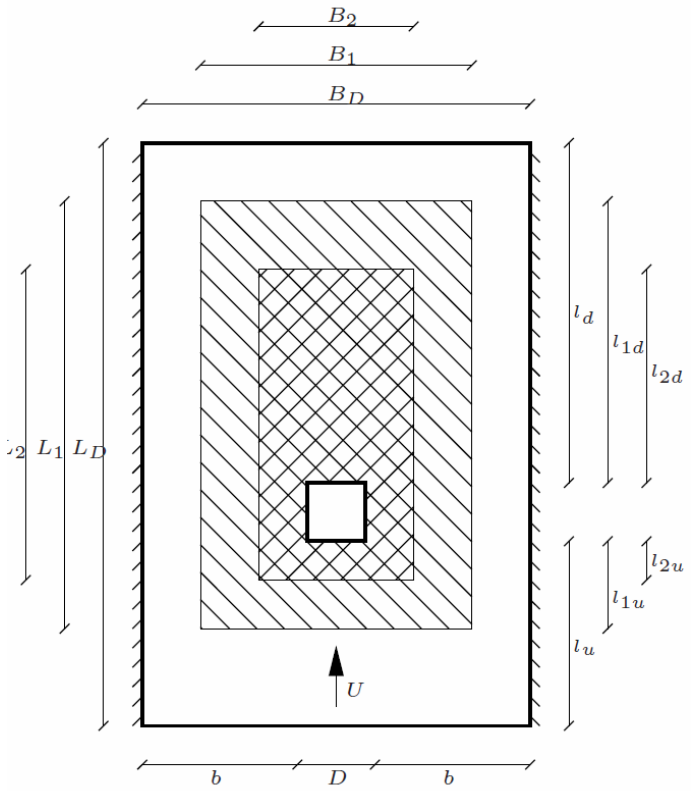

Figure 1 Sketch of the meshing strategy. The computational mesh was set-up with varying degrees of refinement.

Boundary conditions.

The oscillatory flow was generated using a boundary condition where amplitude and frequency of the oscillatory motion specified the velocity on the boundaries. The inlet values for the turbulence model parameters, turbulence intensity I= 0.05 % and length scale L. The pressure define as zero gradient on one inlet/outlet boundary and fixed total pressure on the other.

Wall boundary

The walls of the moonpool and the walls of the structure are set to have no-slip conditions. Wall functions were applied for k and ω. To avoid decomposing the viscous sub-layer and the logarithmic layer close to the walls in the computational domain - which would in many cases require very fine meshes - wall functions can be applied to determine the turbulence parameters and thereby the correct turbulent viscosity near the walls.

A zero gradient was applied for the turbulent kinetic energy k. The wall function the ω was:

$$\omega = \sqrt{\omega_{vis}^2 + \omega_{\log}^2} \tag{1.10}$$

Where:

$$\omega_{vis} = \frac{6\nu}{\beta_1 y^2} \tag{1.11}$$

$$\omega_{\log} = \frac{\sqrt{k}}{C_\mu^{0.25} \kappa y} \tag{1.12}$$

β_1, C_μ and κ are constants and y is the first point from the wall. It is important that the first point away from the wall is placed inside the logarithmic layer. This is ensured by ensuring that the center of the first computational cell has a value of y+ between 30 and 300.

EXPERIMENTAL SET-UP

A 2.5 meter long plate was placed in a channel filled with water to narrow down the width to 280 mm of the experimental section as sketched in Figure 2. The channel defined by the side of the flume and the plate was not closed at the ends in order to avoid reflections from the ends.

A carriage, mounted on rails, forms the basis of mounting the cylinders. In order to move the carriage, a hydraulic double ended cylinder piston was used as seen on Figure 4. To control the movement, a sinusoidal signal was sent to a control box, which controlled a servo valve on top of the piston cylinder. A given electric current signal to the servo valve, resulted in an extension or reduction of the piston relative to neutral position. On the side of the cylinder a LVDT (Linear Variable Differential Transformer) was attached, which was used for feedback to the control box. It let the control box to correct for any false displacement of the piston caused by external forces. This LVDT could not be used for the displacement measurements. Instead, we applied an external string recorder for that. A compressor generated the hydraulic pressure with a working pressure of 100 Bar. This powered the piston with a sufficient amount of force. The periods of the oscillations were of order $T = O(1)s$ and higher. Lower periods would create large forces and velocities that might compromise the safety and the equipment. The computer was set to use an output frequency of 500Hz.

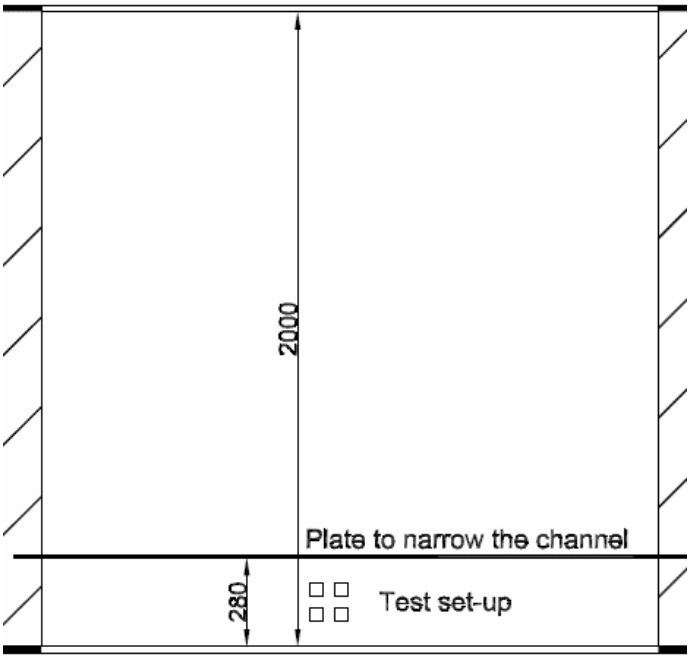

Figure 2 Test section sketched from above in a 2 m wide flume in the hydraulic laboratrory at DTU

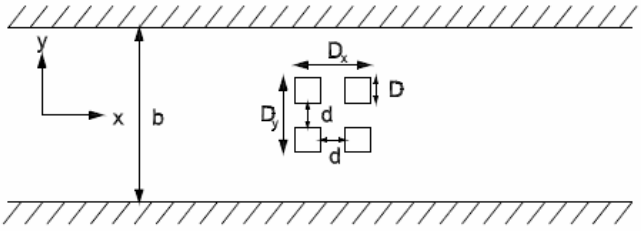

Figure 3 Definition sketch of set-up in narrowed channel

A total of four square cylinders was used, see Figure 3. Each square cylinder consisted of an aluminium part of 40×40 mm sharp edges. A box of transparent polycarbonate was glued to the bottom. The polycarbonate made it possible to shoot the laser sheet through the cylinder to illuminate the particles for the PIV all over the channel width. The mass of a cylinder was roughly 390 grams

The cylinders were attached to the carriage through two load cells; TAL201 from HT-censors with a maximum capacity of 10 kg load at the tip of the load cell. The load cells were mounted together allowing the two load cells to measure loads in directions perpendicular to each other.

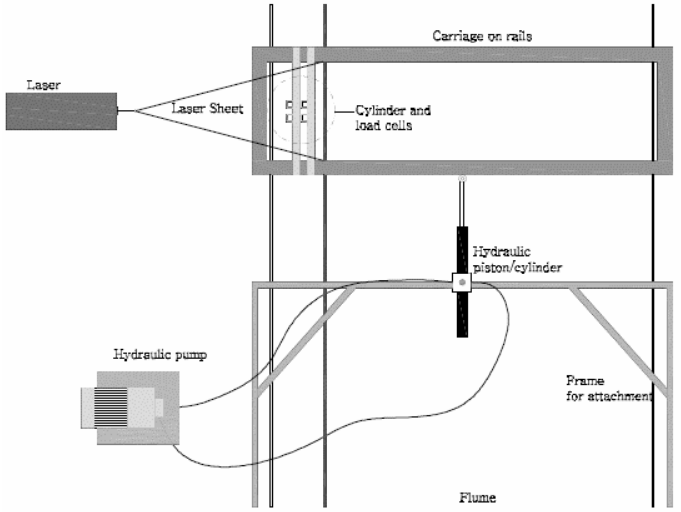

Figure 4 Sketch of the actual set up seen from above. The carriage supports on the rails mounted on the side of the flume.

PIV-system for flow visualization

We used a Dantec laser to establish a laser-sheet. The output proved to be sufficient for PIV recordings of the type needed for this project. It should be mentioned that the laser intensity was on the limit of what was possible for the camera to record with convincing quality. The laser produced a beam of light, which had to be spread out to form a sheet. This was achieved by shooting through a 6mm clear polished polycarbonate cylinder. To obtain enough width for the sheet to illuminate the area of interest, the curvature of the cylinder had to be relative large compared to the diameter of the laser beam. Also by increasing the distance from the cylinder to the area to be illuminated, the laser sheet could be widened.

RESULTS

Model validation

The validation cases are summarized in Table 1. A section of the time series for the in-line force is shown for case 2.8 in Figure 5 along with the Morison fit.

The Morison equation was expressed as:

$$f_{inline} = \tfrac{1}{2}\rho C_D D U|U| + \rho A_{cross.sec} C_M \dot{U} \qquad (1.13)$$

where f_{inline} is the force per unit length, ρ the density, D the side length of the square cylinder, $A_{cross.sec}$ was set equal to the area of a cross-section with a diameter of D, $A_{cross.sec} = \frac{\pi}{4}D^2$. C_D and C_M are force coefficients that has to be found by a best fit procedure, see for instance [11].

The drag and inertia coefficients found from the Morison fit are shown in Figure 6 and Figure 7 where they are compared to experimental data from [12].

Table 1 Validation cases for oscillatory flow around a single square cylinder. Maximum velocity Um, Keulegan-Carpenter number KC, turbulence model parameters I and L for inlet flow, grid size variation, and y+ for the center of the first cell on the cylinder boundary.

Case	U_m	KC	I	L	Grid	y+
	[m/s]	[-]	[-]	[m]	[-]	[cells/m]
2.1	0.002	0.01	0.05	1	12-24-48	1
2.2	0.02	0.1	0.05	1	12	32
2.3	0.15	1	0.05	1	8-16	157
2.4	0.3	2	0.05	1	12-24-48	99
2.5	0.9	6	0.02	1.5	12-24-48-96	138
2.6	1.5	10	0.05	1	10-20-40-80	266
2.7	3	20	0.05	1	10-20-40-80-160	253
2.8	4.5	30	0.05	1	13-26-52-104-208	283

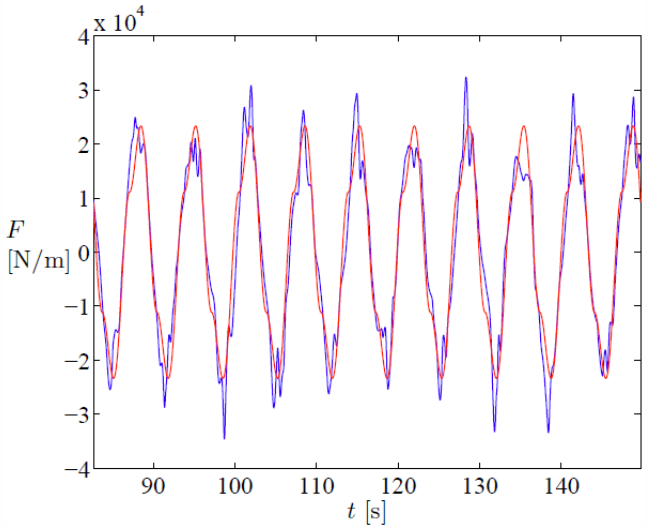

Figure 5 In-line force for validation case 2.8, KC = 30. OpenFOAM result: blue line. Morison fit: red line.

From Figure 6 it is seen that there was an overall acceptable correlation between model results and experimental data for KC values above 1. Results for KC of 0.01 and 0.1 were omitted as the force in these cases will be dominated by the inertia term, and hence the modelling of C_D will be very inaccurate. This effect might also be the reason for the large deviation between experimental and model results seen for $KC = 1$. The results for $KC = 2$, 6 and 10 are all within 0-7 % deviation from experiments. Higher KC values, results in larger deviations as indicated in Figure 6. A reason for this could be insufficient length of the domain in the stream wise direction.

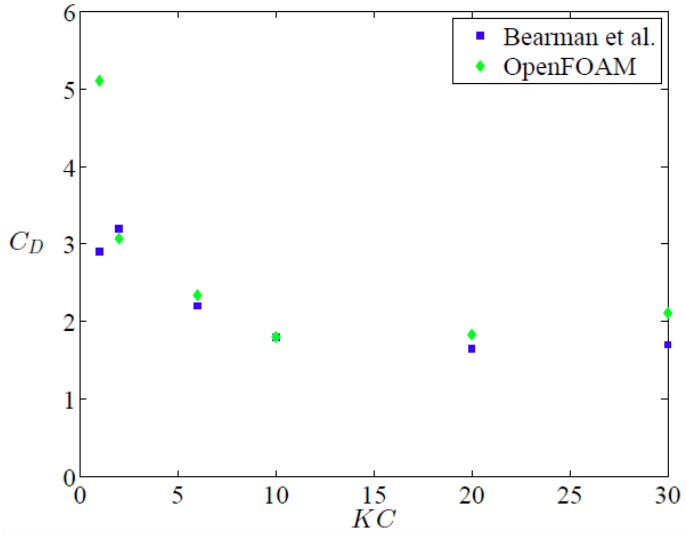

Figure 6 Values obtained for drag coefficient using OpenFOAM compared to experimental values from [12]. KC values 1, 2, 6, 10, 20, 30

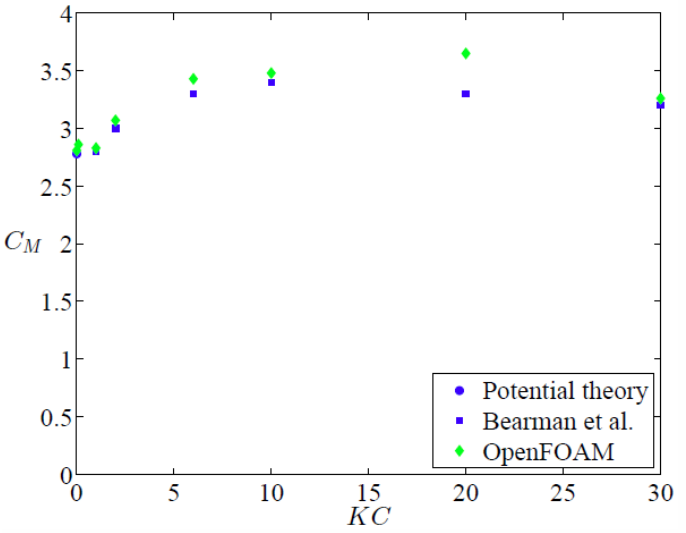

Figure 7 Values obtained for inertia coefficient using OpenFOAM compared to experimental values from [12] and potential theory. KC values 0.01, 0.1, 1, 2, 6, 10, 20, 30.

Figure 7 shows the model results for C_M. For $KC \geq 1$ the results were compared to those found experimentally. For $KC = 0.01$ and 0.1, the comparison was made to the solution from potential flow theory, see [12]. It was seen that all model results are within 1-4 % deviation of the experimental, with the exception of the result for $KC = 20$, which deviated by 11 %. This may either be due to the boundary effects as described

above or to the fact that at this KC level, the force was increasingly drag dominated, making the modelling of the inertia term more uncertain.

The experiments showed approximately the same results as the numerical calculations for the validation case. This gave confidence to the experimental set-up as well.

2x2 case

As a typical complex structure a 2 by 2 configuration is presented in the following. The 2x2 set up in the experiments is sketched in Figure 8. The set up is in principal a simple large scale porous structure of a symmetric kind.

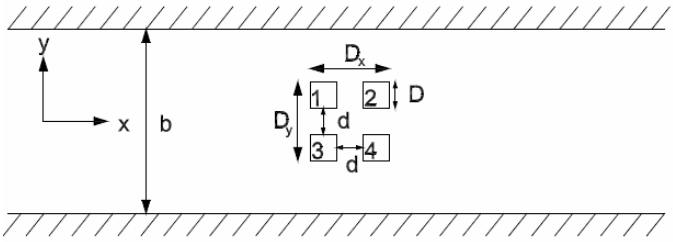

Figure 8 2x2 constellation in 0.28 m channel in the physical experiments.

Two examples of the forces on the four cylinders are given in Figure 9 and Figure 10 that has a spacing between the cylinders of *d/D = 0.5* and *d/D = 1.0*, respectively. Filtering of the measured force signal might have left only the major component of the force, and therefore the results should mainly be used an indication of the force distribution.

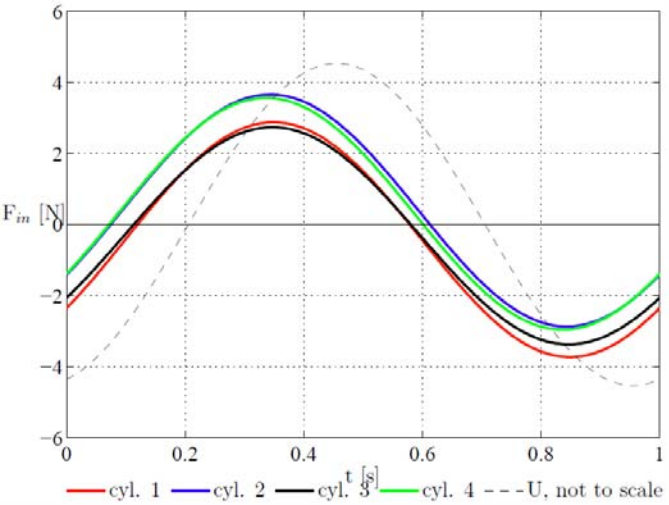

Figure 9 Ensemble average over 180 periods for all cylinders at $KC = 11.3$ for $d/D = 0.5$

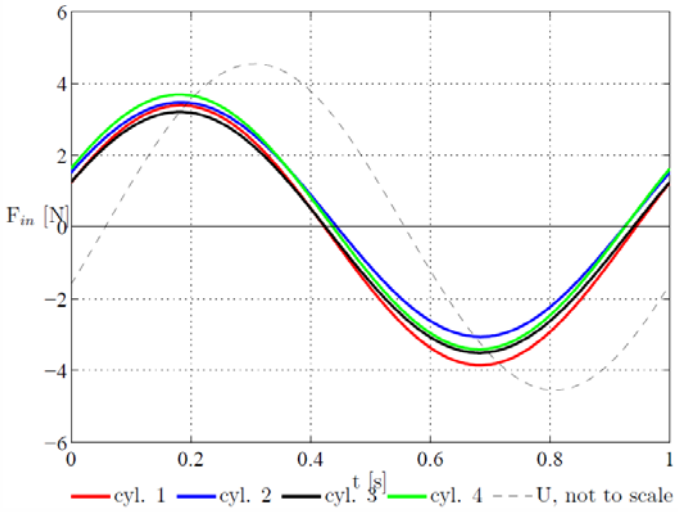

Figure 10 Ensemble average over 180 periods for all cylinders at $KC = 11.3$ for $d/D = 1.0$

In the numerical analyses, the definition of the cylinders was given as sketched in Figure 11.

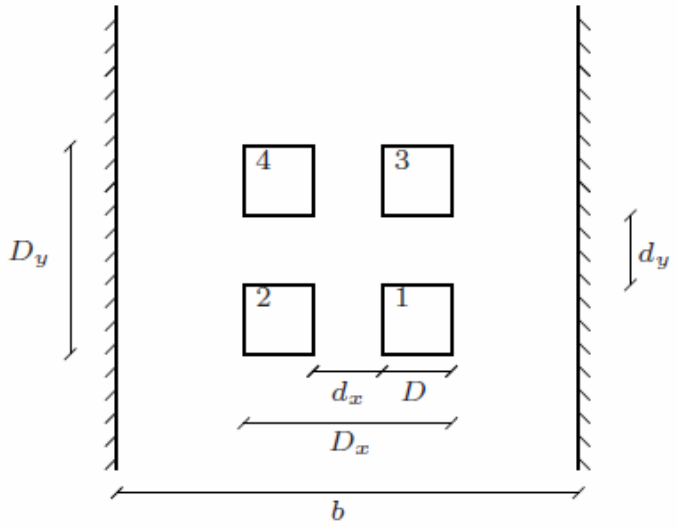

Figure 11 Definition sketch for 2 by 2 cylinders. Cylinder diameter *D*, structure in-line diameter D_y and cross flow diameter D_x, in-line cylinder distance d_y, crossflow cylinder distance d_x and moonpool width *b*.

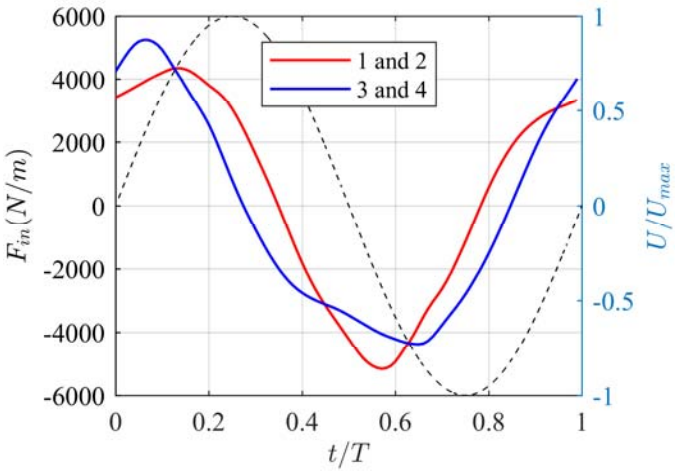

Figure 12 Ensemble average over 14 periods for cylinder pairs. For $KC = 10$ and $d/D = 0.5$.

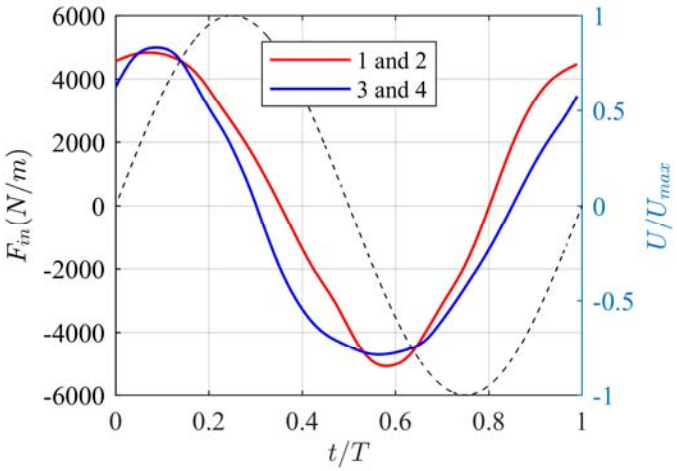

Figure 13 Ensemble average over 14 periods for cylinder pairs. For $KC = 10$ and $d/D = 1.0$.

If we take a closer look on the behavior of the forces found from experimental and numerical analyses it appears that the 2 2 by 2 arrangement introduced an asymmetry. The forces on the individual cylinders were largest when they were to the lee-side of the flow. For instance the cylinders 1 and 3 in the experiment, cf. Figure 8 and Figure 9, the absolute value of the minimum of the force was larger than the maximum of the force. The same effect was observed from the numerical analyses, see Figure 11, Figure 12, and Figure 13. Here an average force was found to each side of the flow, i.e. cylinder 1 and 2, and cylinder 3 and 4. The absolute maximum force was in all cases found on the cylinders to the lee side of the flow, and the effect of this asymmetry decreased with increasing relative distance *d/D*. This appears at fist as contradictory to the idea of a "shielding" effect. In constant current flow the forces on for instance a second cylinder is often smaller than on the front cylinder.

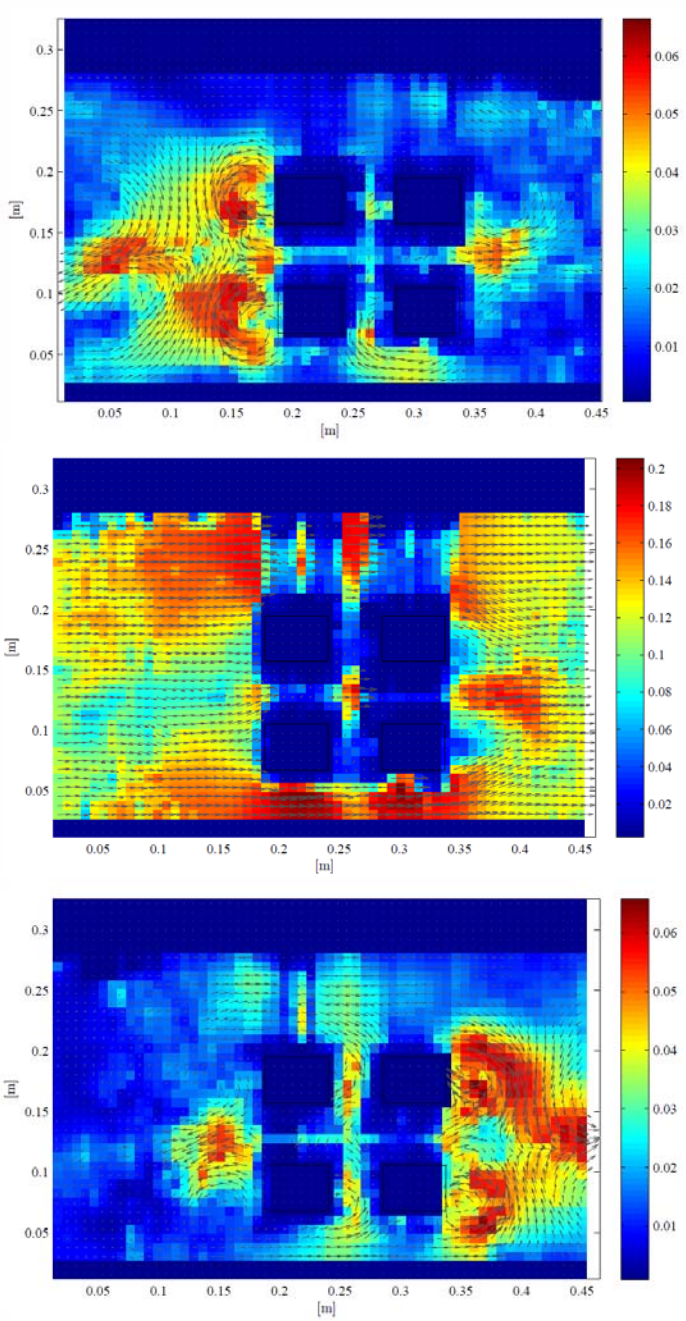

Figure 14 Visualazation of measured velocity field at: Top $\omega t = 0°$, Middle, $\omega t = 90°$, bottom, $\omega t = 180°$. d/D = 1.0, KC = 11.2

Figure 14 shows three cases of the flow for *KC = 11.3* and *d/D = 1.0* from the experiments. First, we have to acknowledge that the square cylinders appears to shadow for the field in the upper part of the figures. However, we can still get a good picture of what happens outside the shadow zones. It is clear that at the change of flow direction relatively large eddies formed on the previous lee-side of the structures, cf. upper and bottom panel. At the maximum outer flow speed, middle panel,

the flow speed was large between the structures where the space acted as a tunnel for the flow. On the lee side of the structure asymmetric wake zones developed.

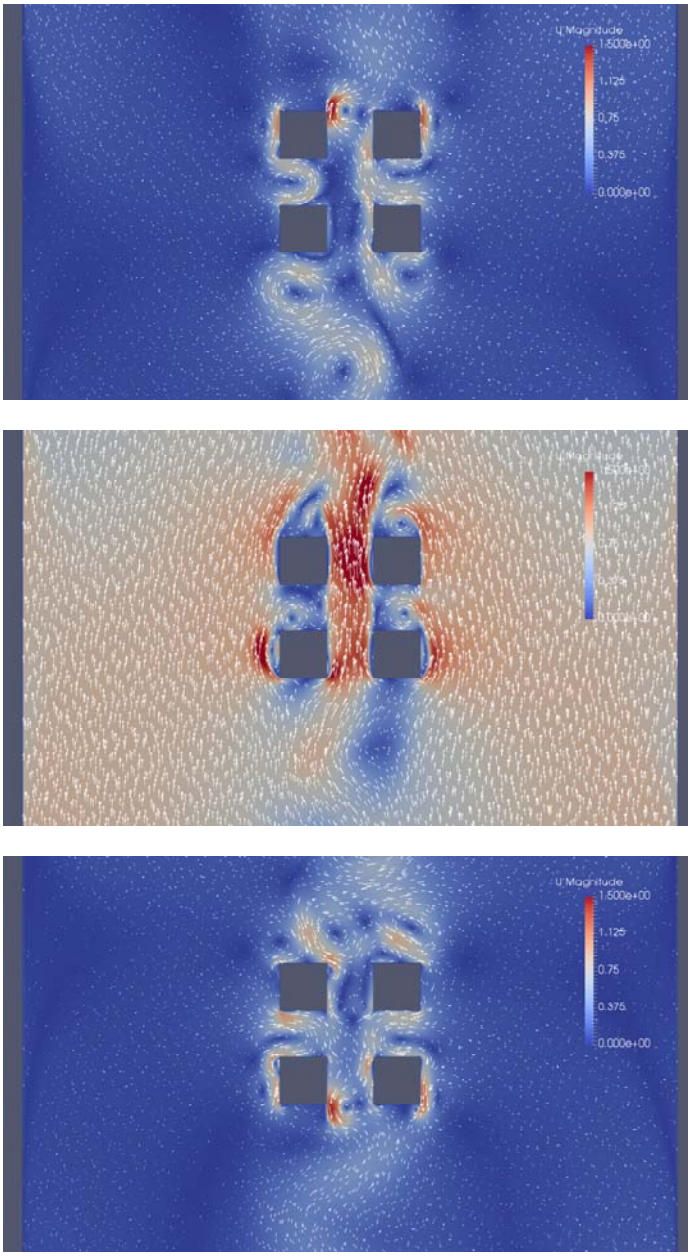

Figure 15 Visualazation of modelled velocity field at: Top $\omega t = 0°$, Middle, $\omega t = 180°$, bottom, $\omega t = 180°$. d/D = 1.0, KC = 10.

The simulated velocity field as shown in Figure 15 had similar characteristics as found from the measurements. Note that the flow in the numerical simulations oscillates in the vertical direction. At the return of the flow at $\omega t = 0°$ and $\omega t = 180°$, relatively strong eddy structures were developed on the previous lee side of the structures. At the maximum outer speed the tunneling effect was very clear as the maximum speed was observed between the structures. The relatively large asymmetric wake zone was also identified from the simulations.

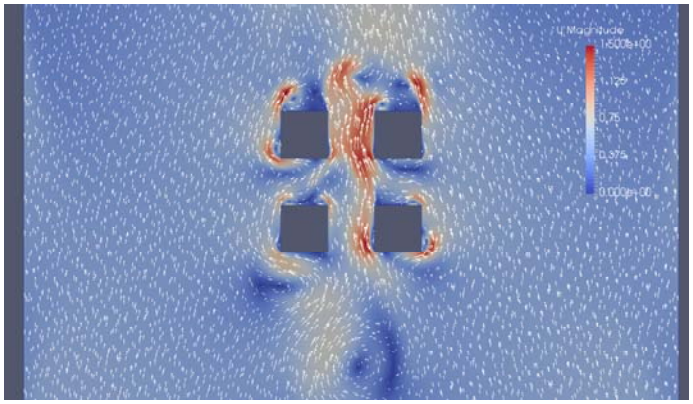

Figure 16 Visualazation of modelled velocity field at: $\omega t \approx 40°$. d/D = 1.0, KC = 10.

In the analyses of the forces we found that maximum force on the cylinders on the instantaneous lee side were larger then on the exposed cylinders. Figure 16 shows the flow field around the cylinders at the time of maximum force. In the figure the upper cylinders is in the lee side of the outer flow direction. The wake zone in this area was already well developed, while the wake zone between the cylinders was at a less developed stage. As wake zones often are related to the separation of the flow and therefore typical a low pressure zone, the well-developed wake in the lee zone will have a significantly effect on the overall force on the cylinder. The other contributions to the force of the cylinder is stagnation pressure on the front (drag-related) and the acceleration of the flow at the front (inertia-related). It could be argued that these contributions appears less well developed compared to the wake zone behind the lee side cylinders. From these observations, we find that the flow fields supports the earlier finding with a maximum force on the lee side cylinder.

Finally, an attempt to estimate the force coefficients in Morisons equation (1.13) based on the numerical simulations. To present the force coefficients in a foreseeable way, the force coefficient are presented as the mean value of the four cylinders along with the standard deviation. From Figure 17 and Figure 18 it is seen that the force coefficient development with KC was overall qualitatively corresponding to that for a single cylinder. It is also seen that the coefficientscients had very small standard deviations, which was expected since theoretically, all four cylinders should be equally exposed to the flow in a 2 by 2 symmetric set-up. The force coefficient dependence with KC qualitatively corresponded to that for a single cylinder. The standard deviation between the forces was in general low as would be expected due to the symmetrical 2 by 2 set-up. The force coefficients increased with increased distance. An explanation for this could be a higher effective blockage effect. In [13] forces on four cylinders in oscillatory

flow were studied without the confinement of the moonpool walls, and their results showed that the force coefficients reduced with increasing spacing.

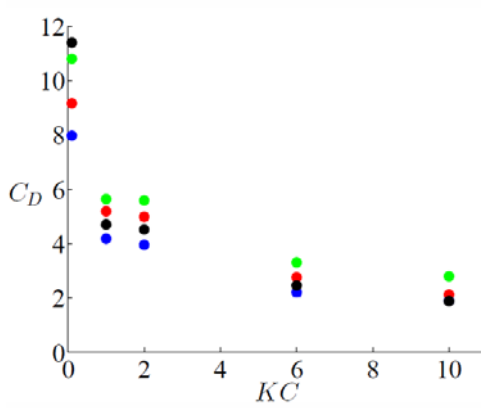

Figure 17 Mean C_D for individual cylinders with placed in a 2x2 configuration. As function of Keulegan-Carpenter number. ●: $d_x / D = d_y / D = 0.5$, ●: $d_x / D = d_y / D = 1.0$, ●: $d_x / D = d_y / D = 2.0$, ●: Single cylinder in $b / D = 7$ moon-pool. Standard deviations are marked with bars.

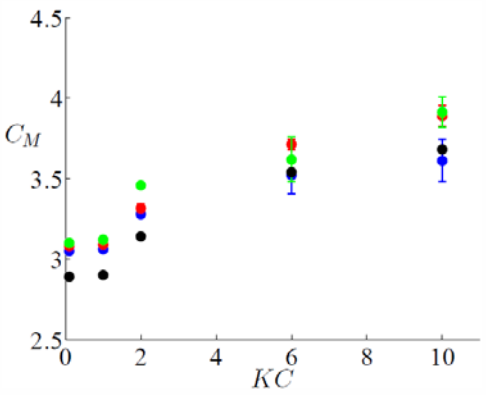

Figure 18 Mean C_M for individual cylinders with placed in a 2x2 configuration. As function of Keulegan-Carpenter number. ●: $d_x / D = d_y / D = 0.5$, ●: $d_x / D = d_y / D = 1.0$, ●: $d_x / D = d_y / D = 2.0$, ●: Single cylinder in $b / D = 7$ moon-pool. Standard deviations are marked with bars.

SUMMARY AND CONCLUSIONS

Two-dimensional numerical experiments have been performed to investigate the inline forces exerted on complex structures placed in a moonpool experiencing resonant piston mode sloshing. These analyses were supported by experimental tests. A good agreement between numerical and experimental forces for a single cylinder with literature, [12], was found.

The complex structures were modelled as clusters of square cylinders in a variety of arrangements. In this paper we focused on the 2 by 2 arrangement. The oscillatory flow in the moonpool was simulated by placing the structures in a tunnel with forced sinusoidally oscillating flow. The tunnel was given a width of 7 m, representing a typical moonpool dimension, and an extent sufficiently long to avoid boundary effects. The period of the oscillatory flow was 6.7 s. The Keulegan-Carpenter number varied up to KC = 10 for a single square cylinder in the numerical analyses. Results were presented in terms of drag and inertia coefficients found by a Morison fit to the numerical force time series.

The upstream cylinder provides shielding for the down stream cylinder. The effect of this was a bit counter intuitive as the downstream cylinder experiences larger forces. This observation was clear from both measurements and numerical simulations. It could be argued that the effect was related to a relative well-developed wake zone on the lee side of the downstream cylinders The shielding creates a region of slow moving water between the cylinder. The shielding effect decreases with increasing gap-ratio making the overall forces on the cylinder to increase with gap-ratio and the two cylinder mean forces approach each other in magnitude. The effect of interaction is almost gone for the widest gap-ratio of *d/D = 2*.

NOMENCLATURE

$A_{cross.sec}$:	Area of cross-section
B_D:	Width of moonpool in numerical analyses
b:	Width of channel/moonpool in experiments
C_D :	Drag force coefficient
C_M :	Inertia force coefficient
d:	Spacing between cylinders
d_x:	Spacing between cylinders in x-direction
d_y:	Spacing between cylinders in y-direction
D :	Diameter of cylinder
D_x :	Total dimension of structure x-direction
D_y :	Total dimension of structure y-direction
F_{in}:	Inline force on a square cylinder
f_{inline}:	Inline force per unit length
I:	Inlet turbulence intensity
k:	Turbulent kinetic energy
KC:	Keulegan-Carpenter number
L:	Length scale of turbulence at inlet
L_D:	Length of moonpool in numerical analyses
ω :	Specific dissipation rate
ω :	Angular frequency
p:	Pressure
ρ:	Density of water
T:	Time period of oscillations
t:	Time
τ_{ij} :	Shear stress tensor
U_i :	The velocity in tensor notation
U_m :	Maximum velocity
μ :	Dynamic viscosity

μ_t :	Dynamic eddy viscosity
ν:	Kinematic viscosity
ν_t:	Eddy viscosity
x_i:	Spatial coordinates
y^+:	Dimensionless distance to the wall

REFERENCES

[1] N. Duncan, ROVs and Moonpools - An Operator's Viewpoint. In: ROV '86: Remotely Operated Vehicles. Springer, Dordrecht, in: ROV '86 Remote. Oper. Veh. Springer, Dordr., 1986: pp. 41–50.

[2] B. Molin, On the piston and sloshing modes in moonpools, J. Fluid Mech. 430 (2001) 27–50. doi:10.1017/S0022112000002871.

[3] O.M. Faltinsen, A.N. Timokha, Sloshing, 2009. www.cambridge.org.

[4] T. Kristiansen, O.M. Faltinsen, Gap resonance analyzed by a new domain-decomposition method combining potential and viscous flow, Appl. Ocean Res. 34 (2012) 198–208. doi:10.1016/j.apor.2011.07.001.

[5] T. Kristiansen, T. Sauder, R. Firoozkoohi, Validation of a Hybrid Code Combining Potential and Viscous Flow With Application to 3D Moonpool, in: Int. Conf. Ocean. Offshore Arct. Eng., 2013: p. 10748. doi:10.1115/OMAE2013-10748.Download.

[6] B. Jensen, N.G. Jacobsen, E.D. Christensen, Investigations on the porous media equations and resistance coefficients for coastal structures, Coast. Eng. 84 (2014) 56–72. doi:10.1016/j.coastaleng.2013.11.004.

[7] E. HORI, Experiments on flow around a pair of parallel circular cylinders, in: Proc. 9th Japan Natl Congr. Appl. Mech., Tokyo, Tokyo, 1959: pp. 231–234.

[8] E.D. Christensen, J. Buhrkall, M.C.D. Eskesen, B. Jensen, ANALYSES OF CURRENT AND WAVE FORCES ON VELOCITY CAPS, in: ASME (Ed.), ASME 2015 34th Int. Conf. Ocean. Offshore Arct. Eng., St. John's, Newfoundland, Canada, 2015: pp. 1–10.

[9] F.R. Menter, Zonal Two-Equation Kappa-Omega Turbulence Model for Aerodynamic Flows, in: AIAA 24th Fluid Dyn. Conf. July 6–9, Orlando, Florida., 1993: pp. 93–2906.

[10] F. Bjørke, Numerical study of hydrodynamic forces on complex structures with application to objects in moonpool, Technical University of Denmark, 2015.

[11] B.M. Sumer, J. Fredsøe, Hydrodynamics Around Cylindrical Structures (Revised Edition), World Scientific Publishing Co. Pte. Ltd., New Jersey. London, Singapore, Beijing, Shanhai, Hong Kong, Taipei, Chennai, 2006. doi:10.1142/9789812772770.

[12] P.W. Bearman, J.M.R. Graham, E.D. Obasaju, G.M. Drossopoulos, The influence of corner radius on the forces experienced by cylindrical bluff bodies in oscillatory flow, Appl. Ocean Res. 6 (1984) 83–89. doi:10.1016/0141-1187(84)90045-2.

[13] P. Anagnostopoulos, C. Dikarou, Numerical simulation of viscous oscillatory flow past four cylinders in square arrangement, J. Fluids Struct. 27 (2011) 212–232. doi:10.1016/j.jfluidstructs.2010.10.005.